Neutron scattering and crystal field studies of the rare earth double perovskite Ba_2ErSbO_6

2010 J. Phys.: Condens. Matter 22 116007

(http://iopscience.iop.org/0953-8984/22/11/116007)

IOP Publishing Journal of Physics: Condensed Matter

J. Phys.: Condens. Matter **22** (2010) 116007 (7pp) doi:10.1088/0953-8984/22/11/116007

Neutron scattering and crystal field studies of the rare earth double perovskite Ba_2ErSbO_6

S Calder[1], T Fennell[2], W Kockelmann[3], G C Lau[4], R J Cava[4] and S T Bramwell[1]

[1] London Centre for Nanotechnology, University College London, 17-19 Gordon Street, London WC1H 0AH, UK
[2] Institut Laue-Langevin, 6 rue Jules Horowitz, BP 156, 38042 Grenoble Cedex 9, France
[3] ISIS Facility, Rutherford Appleton Laboratory, Chilton, Didcot, Oxfordshire OX11 0QX, UK
[4] Department of Chemistry and Princeton Materials Institute, Princeton University, Princeton, NJ 08540, USA

E-mail: s.calder@ucl.ac.uk

Received 19 December 2009
Published 5 March 2010
Online at stacks.iop.org/JPhysCM/22/116007

Abstract

The rare earth double perovskite Ba_2ErSbO_6 contains an ordered face-centred cubic lattice of Er^{3+} ions, suggesting that this material is a candidate for showing the effects of geometric magnetic frustration. Crystal field effects have also been shown to be important in this series. We report a systematic experimental study involving neutron scattering and bulk measurements that show no evidence of long ranged magnetic order or spin glass freezing down to 70 mK. A description of the system in terms of a crystal field scheme is established from inelastic neutron scattering. These measurements rule out significant magnetic coupling and show that all observed properties are fully explained by a model of uncoupled magnetic Er^{3+} ions.

(Some figures in this article are in colour only in the electronic version)

1. Introduction

The concept of geometric magnetic frustration has led to the discovery of a variety of novel low temperature spin states including spin liquid and spin ice [1–3]. These states are generally formed by systems in which the magnetic ions reside at the corners of triangular or tetrahedral units which frustrate the magnetic interactions. For example, the rare earth pyrochlores, with lattices of corner sharing tetrahedra, have been the subject of many investigations into frustrated magnetism.

The search for new model systems has led to the recent consideration of the face-centred cubic (fcc) lattice and in particular the rare earth double perovskites [4, 5]. The magnetic ions occupy a lattice with one of the simplest frustrating geometries and as such lend themselves well to theoretical studies. The fcc lattice is typically drawn to emphasize its cubic symmetry but can equivalently be drawn to display the edge sharing tetrahedral structure with each site having 12 nearest-neighbours (figure 1).

Spins on an fcc lattice with nearest-neighbour antiferromagnetic interactions are therefore frustrated, with an infinite degeneracy of ground states [6]. For classical spins, the ground state degeneracy is thought to be lifted by thermal fluctuations [7], leading to a first order phase transition at finite temperature [8, 9]. For Heisenberg spins with nearest-neighbour coupling only, quantum fluctuations of the transverse spin component may however destabilize long range order in favour of a spin liquid state [10]. However, no experimental examples of highly correlated but disordered state, such as a spin liquid, have been found on the fcc lattice of the double perovskites.

Ba_2HoSbO_6 has been previously investigated and was found to have a non-magnetic ground state that precluded the development of long or short range magnetic order [5]. In this new study, Ba_2ErSbO_6 is investigated, which has a non-integer J angular momentum value and as such necessarily has a magnetic ground state in the crystalline electric field (CEF).

The CEF has proved to be a crucial factor in the description of the magnetic properties of rare earth salts. It

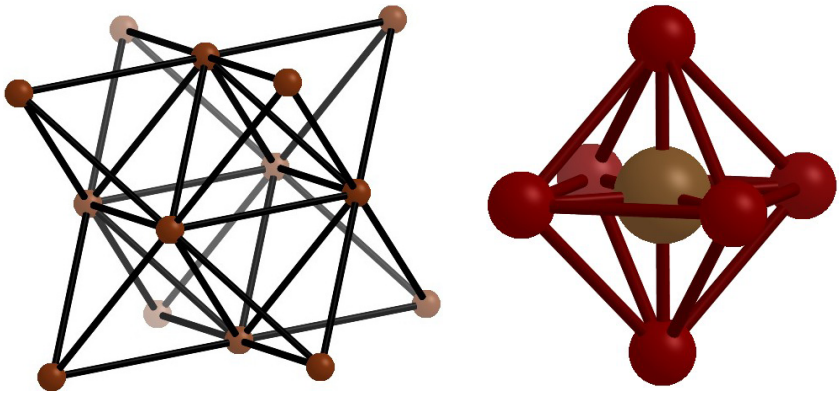

Figure 1. (Left) The rare earth ions in Ba_2ErSbO_6 sit on the corners of edge sharing tetrahedra in an fcc lattice. Each rare earth ion is connected to twelve nearest-neighbours resulting in a highly connected lattice. (Right) The rare earth ion surrounded by six oxygen ions in an octahedral coordination.

is the CEF at the lanthanide site that determines the electronic states of the single rare earth ion. For example, in the case of the elpasolite series A_2BLnX_6 [11–17] (A, B = Li, Na, K, Rb, and Cs; Ln is a lanthanide; X = F, Cl), which also contains an fcc lattice of rare earth ions, CEF effects generally dominate those arising from magnetic coupling. For non-Kramers ions the materials behave as Van Vleck paramagnets with a non-magnetic ground state, while for Kramers ions, the systems order at low temperature.

A detailed investigation is presented here of the rare earth double perovskite Ba_2ErSbO_6 through susceptibility measurements, inelastic neutron scattering, neutron powder diffraction and polarized neutron analysis. No long or short range magnetic order is observed. This is well explained by the CEF level scheme deduced here. The excellent agreement of the CEF model with the experimental results leads to the conclusion that the Er^{3+} ions in Ba_2ErSbO_6 behave as uncoupled ions in which the CEF dominates any exchange or dipolar coupling in the system in the temperature regime investigated.

2. Experimental methods

The preparation and initial characterization of polycrystalline Ba_2ErSbO_6 were carried out as described elsewhere [4]. DC magnetization (M) was measured with a Quantum Design Superconducting Interference Device (SQUID) magnetometer between room temperature and 1.7 K. Powder neutron diffraction measurements were carried out at the ISIS pulsed neutron source using the high intensity and high resolution diffractometer GEM between 20 and 1.5 K. A xyz neutron polarization analysis was performed on the D7 instrument at the ILL for the temperature range 0.07–5 K and an inelastic neutron scattering experiment was carried out at ISIS using the MARI spectrometer between ambient temperature and 5 K.

3. Experimental results

3.1. DC magnetic susceptibility measurements

No susceptibilty measurements for Ba_2ErSbO_6 have been reported in the literature so measurements were carried out to test for any ordering within the sample down to 1.7 K.

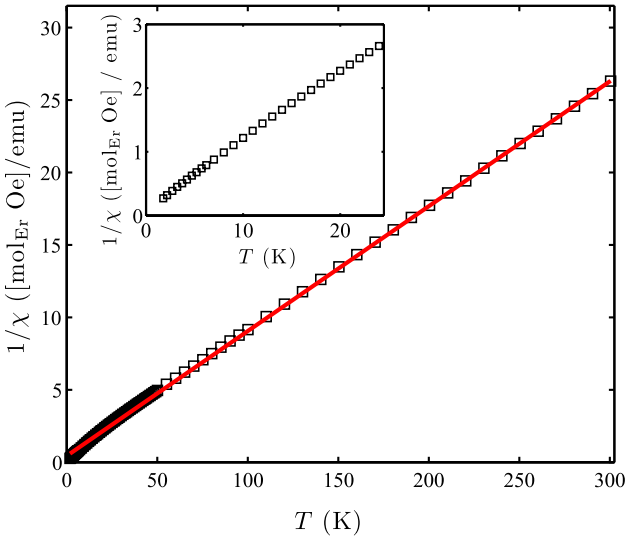

Figure 2. Experimental dc magnetic susceptibility (M/H) as a function of temperature in a 100 Oe applied field (squares). FC and ZFC results are identical. The straight line is a fit to the Curie–Weiss law in the region 100–300 K with $\theta_W = -5.1$ and moment of 10.8 μ_B/Er.

Table 1. Parameters from GSAS refinement for 20 K for Ba_2ErSbO_6.

Ba	$(x, y, z) = 0.25\ 0.25\ 0.25$	$U_{iso} = 0.002(1)$
Er	$(x, y, z) = 0\ 0\ 0$	$U_{iso} = 0.0009(6)$
Sb	$(x, y, z) = 0.5\ 0.5\ 0.5$	$U_{iso} = 0.001(1)$
O	$(x, y, z) = 0.263(2)\ 0\ 0$	$U_{iso} = 0.003(7)$
	$a(= b = c)$	8.3904(3) Å
	Space group	$Fm\bar{3}m$
	χ^2	5.834

The results of field-cooled and zero-field-cooled measurements of the temperature dependence of the magnetization (M) shows no anomalies corresponding to long ranged magnetic ordering or spin glass freezing down to $T = 1.7$ K: see figure 2. The high temperature results between 100 and 300 K are fitted well to the Curie–Weiss law with $\theta_W = -5.1$ K and

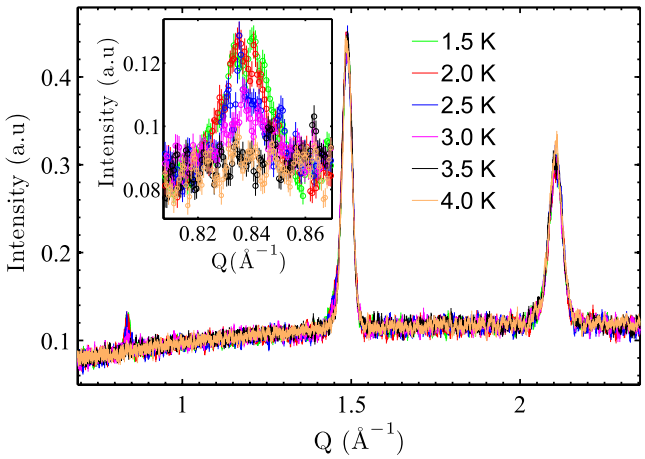

Figure 3. Development of magnetic order in the Ba_2ErSbO_6 powder sample. The inset shows the order develops between 3.0 and 3.5 K. This corresponds to the magnetic ordering temperature of Er_2O_3 of 3.4 K [18].

a moment of 10.8 μ_B/Er. The lack of ordering around the Weiss temperature is often interpreted as being indicative of a frustrated system.

3.2. Powder neutron diffraction

Neutron powder diffraction measurements were carried out using the GEM diffractometer at ISIS. The results collected at 20 and 1.5 K were refined using GSAS starting from the lattice parameters reported in the literature for diffraction experiments on Ba_2ErSbO_6 [19]. The refined crystallographic model gave a good agreement with the experimental data for the results obtained at 20 K (see table 1). A similar good agreement could be obtained for the low temperature 1.5 K results. Close inspection, however, of the difference between 20 and 1.5 K diffraction results indicate an increase in Bragg scattering at low temperature. This is attributed to magnetic ordering. A temperature scan down to 1.5 K is shown in figure 3. As can be seen the onset of magnetic order occurs around 3.5 K. The size of the magnetic peaks relative to the nuclear peaks (<10%) suggests an impurity phase of similar fraction. Using an impurity phase of Er_2O_3 in the GSAS refinement at 1.5 K allows the magnetic reflections to be indexed: see figure 4. Er_2O_3 was one of the starting materials in the chemical synthesis, explaining its presence in the final powder sample. The magnetic ordering temperature of Er_2O_3 is 3.4 K [18] and as such is fully consistent with the results. A small impurity phase is also consistent with the seemingly pure paramagnetic behaviour of the sample observed in magnetometry. All nuclear Bragg peaks at 20 and 1.5 K fit the two phase model of Ba_2ErSbO_6 and Er_2O_3, as shown in figure 5.

3.3. Polarized neutron analysis

The low temperature neutron investigation was extended down to 70 mK. In order to gain information on any diffuse or short range order neutron polarization analysis was carried out on D7 at the ILL. So called 'xyz' analysis allows the complete

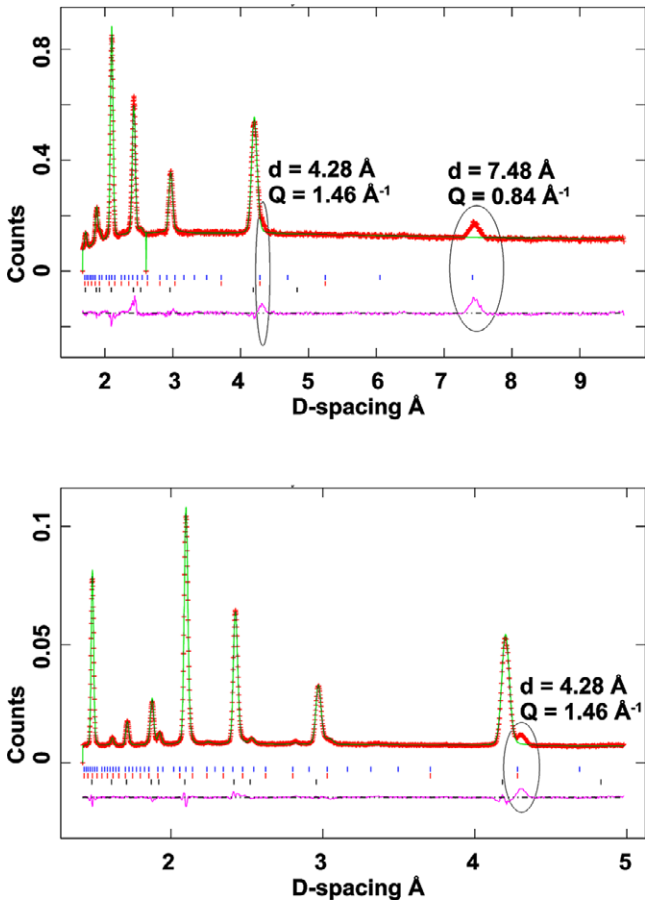

Figure 4. Neutron diffraction profile corresponding to the GSAS refinement of the crystal structure for Ba_2ErSbO_6 at 1.5 K using an impurity phase of Er_2O_3. The three reflection ticks from top to bottom represent magnetic Er_2O_3, nuclear Er_2O_3 and nuclear Ba_2ErSbO_6 phases. The most obvious magnetic peaks are circled and shown to be all indexed by a magnetic Er_2O_3 phase. The crosses are the experimental data and the solid green line is the calculated diffraction with the difference plot shown; the Er_2O_3 phase fraction is 1.8%.

separation of the various nuclear and magnetic contributions to the scattering that combine to give the total scattering observed in standard diffraction such as that performed on GEM. This technique is therefore extremely powerful in obtaining unequivocal magnetic information, as the coherent magnetic scattering arising from electronic magnetic moments can be isolated (henceforth we simply call this 'the magnetic scattering').

The results of the separated magnetic component for Ba_2ErSbO_6 is shown in figure 6. Apart from the indicated peaks which are due to the Er_2O_3 discussed there is no sign of diffuse correlations or long range order. Starting from empirical analytical formulae and using relevant coefficients [20] the magnetic form factor for Er^{3+} was least squares fitted to the magnetic neutron scattering. As shown in figure 6, the magnetic scattering closely follows the form factor squared of Er^{3+}, with no variation between 70 mK and 5 K. This shows that there are no spin–spin correlations within the fcc lattice of Ba_2ErSbO_6 despite a negative Weiss temperature of ∼5 K.

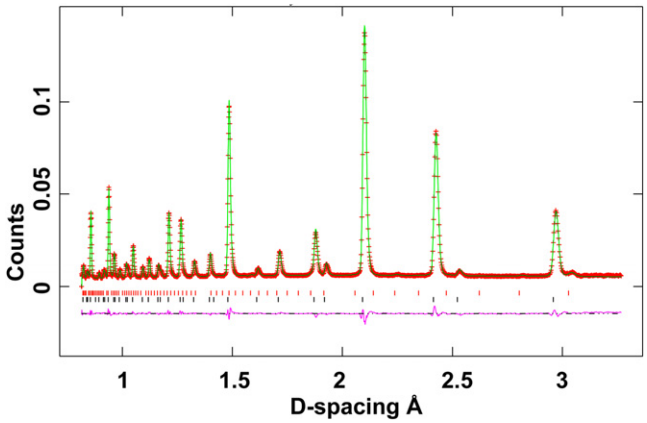

Figure 5. Neutron diffraction profile corresponding to the GSAS refinement of the crystal structure of Ba_2ErSbO_6 at 20 K, including a 1.8% impurity phase of Er_2O_3. The two reflection ticks from top to bottom represent nuclear Er_2O_3 and nuclear Ba_2ErSbO_6 phases. The unindexed peaks are now fitted to nuclear scattering of Er_2O_3.

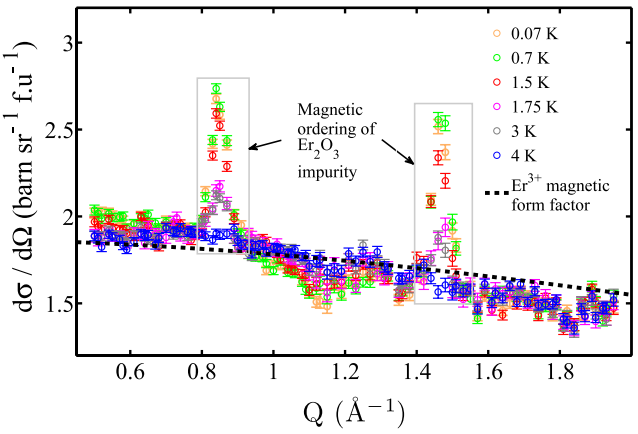

Figure 6. Magnetic scattering from Ba_2ErSbO_6 determined by xyz neutron polarization analysis, using D7 at the ILL. No magnetic long or short range order is evident and the $|Q|$ dependent scattering fits the form factor for Er^{3+} between 4 and 0.07 K. The observed magnetic peaks arise from an impurity phase of Er_2O_3.

3.4. Inelastic neutron scattering

The CEF has proven to be key to interpreting the magnetic behaviour of the related compound Ba_2HoSbO_6 and so to gain further information on Ba_2ErSbO_6, inelastic neutron scattering experiments were carried out to determine the CEF level scheme. The experiment was conducted on the MARI spectrometer at ISIS. Figure 7 shows the inelastic neutron data at $T = 5$ and 200 K with initial neutron energies of 8, 35 and 75 meV. The implications of these results will be discussed below.

4. Analysis and discussion

4.1. Crystalline electric field

The crystal field Hamiltonian can be expressed as

$$H_{\mathrm{CEF}} = \sum_{nm} B_n^m O_n^m, \tag{1}$$

where O_n^m are Stevens' operators acting on the J angular momentum states and B_n^m are the CEF parameters [21]. The symmetry at the site of the rare earth ion under investigation determines which of the terms in H_{CEF} are non-zero. For the site of cubic symmetry, $m3m$, of the Er^{3+} ions in Ba_2ErSbO_6 there are only four terms in the crystal field Hamiltonian. Furthermore, there is a simple relation between the two fourth order terms and the two sixth order terms. Therefore only two parameters B_4 and B_6 are sufficient to describe the CEF. H_{CEF} is written as follows:

$$H_{\mathrm{CEF}} = B_4^0[O_4^0 + 5O_4^4] + B_6^0[O_6^0 - 21O_6^4]. \tag{2}$$

To determine the crystal field parameters from neutron spectroscopy it is convenient to make use of the results of Lea, Leask and Wolf (LLW) [22] wherein the normalized eigenvectors and eigenvalues for all integer and half integer J values between 2 and 8 were tabulated using all possible values of the ratio between the two crystal field parameters. In this way the problem of finding values for the crystal field parameters in cubic symmetry is reduced to a one-dimensional problem, without approximation.

They achieve this by rewriting equation (2) in the following form:

$$H_{\mathrm{CEF}} = B_4^0 F(4)\frac{O_4^0 + 5O_4^4}{F(4)} + B_6^0 F(6)\frac{O_6^0 - 21O_6^4}{F(6)}, \tag{3}$$

where $F(4)$ and $F(6)$ are constant factors for a particular J. To cover all the possible values of the ratio between B_4 and B_6 LLW set:

$$B_4^0 F(4) = Wx \tag{4}$$

$$B_6^0 F(6) = W(1 - |x|), \tag{5}$$

where $-1 \leqslant x \leqslant 1$ and W is introduced in these equations as an energy scale factor between $-\infty \leqslant W \leqslant \infty$ for the crystal field energy levels. The CEF parameters can then be found by scanning for possible values that match the pattern of the peaks from neutron spectroscopy, and then applying an appropriate energy scaling value W, where these values are entirely equivalent to the B_4 and B_6 parameters. All the possible x positions from the LLW plots that could be realistically matched to the spectra of peaks were used to find and verify a fit to the data. Ultimately it was found that only one region, around $x = 0.8$, allowed a close fit to peak position and intensity along with the peak variation with temperature. Using the least squared fitting package FOCUS [23], we find that $x = 0.799$ and $W = 0.134$ meV provides the best fit to the inelastic neutron scattering data for all temperatures measured between 300 and 5 K (figure 7), as shown by the solid curves. It should be noted that the small inelastic peak observable around 5 meV is due to the impurity phase of Er_2O_3 with results in the literature showing a CEF level at 5 meV for Er_2O_3 [24–26].

The CEF parameters for Er^{3+} in Ba_2ErSbO_6 are therefore found to be

$$B_4^0 = 0.179 \times 10^{-2}\ \mathrm{meV}$$

$$B_6^0 = 0.194 \times 10^{-5}\ \mathrm{meV},$$

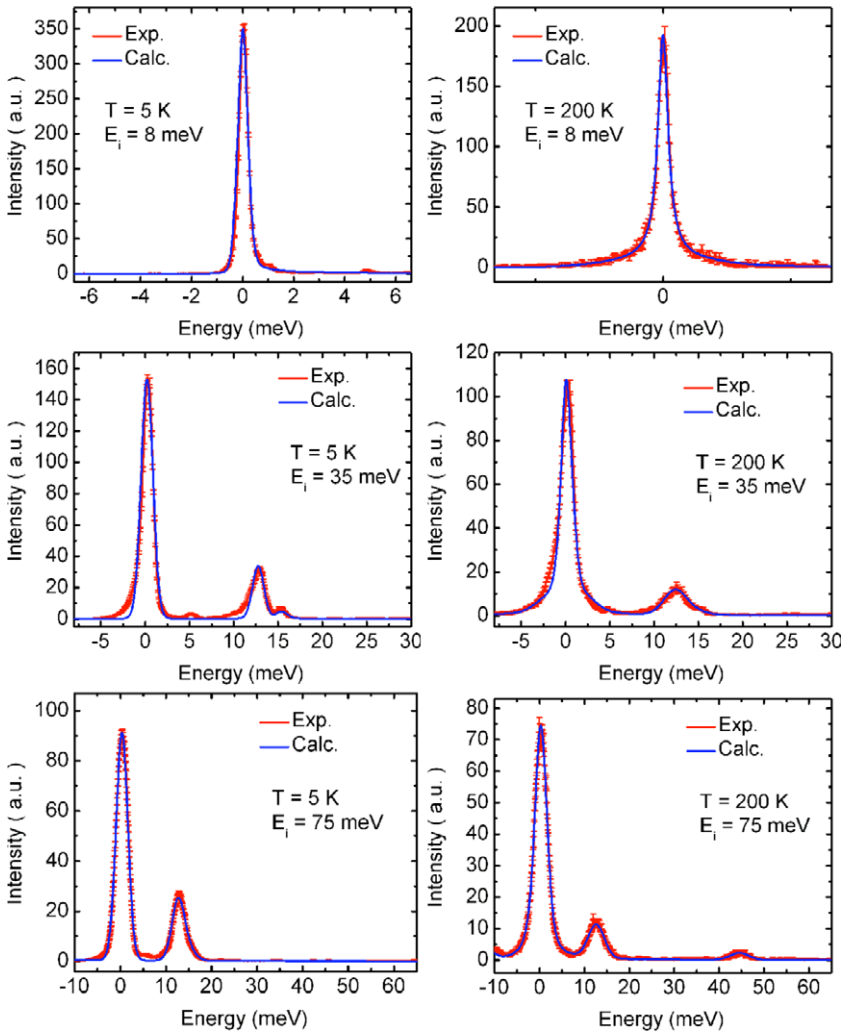

Figure 7. The solid line shows the best fit of the INS data (crosses) using the FOCUS fitting package [23]. The fits were obtained using the same crystal field parameters of $B_4^0 = 0.179 \times 10^{-2}$ meV and $B_6^0 = 0.194 \times 10^{-5}$ meV throughout.

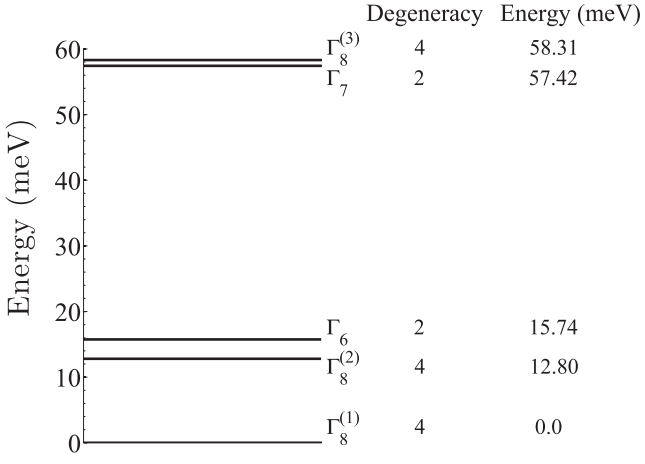

Figure 8. Predict CEF level scheme for Er^{3+} in Ba_2ErSbO_6.

with an error of $\pm 0.007 \times 10^{-2}$ and $\pm 0.007 \times 10^{-5}$ on B_4^0 and B_6^0, respectively. The resultant CEF level scheme is shown in figure 8 and the corresponding wavefunctions in table 2.

4.2. Calculation of susceptibility from CEF parameters

Using the wavefunctions and energies tabulated by LLW for compounds with cubic symmetry, one can calculate the magnetic susceptibility using the Van Vleck formula [27]:

$$\chi = \frac{Ng_J^2\mu_B^2}{Qk_BT}\left[\sum_i |\langle\Gamma_i|J_z|\Gamma_i|\rangle|^2 \exp\left(\frac{-E_i}{k_BT}\right)\right] + \frac{2Ng_J^2\mu_B^2}{Q}\left[\sum_{i,j} \frac{|\langle\Gamma_i|J_z|\Gamma_j|\rangle|^2}{E_j - E_i} \exp\left(\frac{-E_i}{k_BT}\right)\right] \quad (6)$$

and the zero field partition function,

$$Q = \sum_i g_i \exp\left(\frac{-E_i}{k_BT}\right), \quad (7)$$

where N is Avogadro's number, J_z the z-component of the total angular momentum J. $|\Gamma_i\rangle$ are the eigenstates of the Hamiltonian which has energy given by E_i where the number of identical terms are taken account by introducing a degeneracy factor.

The calculated susceptibility for Ba_2ErSbO_6 is shown by the red curve in figure 9(a), which is in excellent agreement

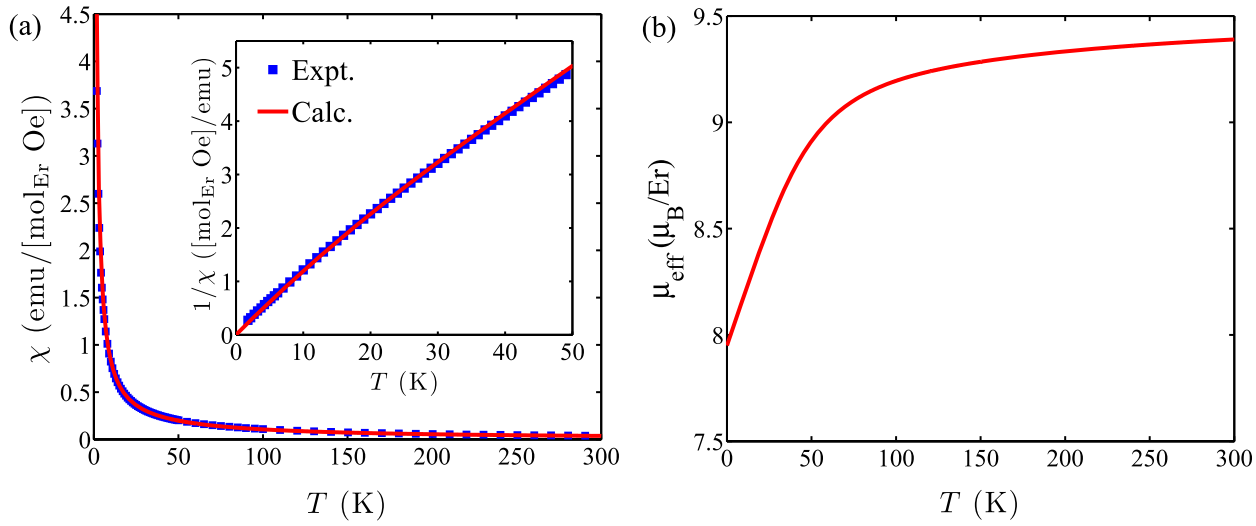

Figure 9. (a) Magnetic susceptibility for Ba_2ErSbO_6 calculated from the crystal field parameters compared with SQUID results. (b) Effective moment calculated from the magnetic susceptibility. The magnetic moment is not zero at 0 K due to Er^{3+} having a magnetic ground state.

Table 2. Wavefunctions and eigenvalues for the CEF level scheme of Er^{3+} in Ba_2ErSbO_6.

Wavefunction	E (meV)
$\Gamma_8^{(3)}(a) = 0.026\|-\frac{13}{2}\rangle + 0.617\|-\frac{5}{2}\rangle + 0.004\|-\frac{3}{2}\rangle + 0.780\|\frac{3}{2}\rangle + 0.003\|\frac{5}{2}\rangle + 0.100\|\frac{11}{2}\rangle$	58.31
$\Gamma_8^{(3)}(b) = 0.100\|-\frac{11}{2}\rangle - 0.003\|-\frac{5}{2}\rangle + 0.780\|-\frac{3}{2}\rangle - 0.004\|\frac{3}{2}\rangle + 0.617\|\frac{5}{2}\rangle + 0.026\|\frac{13}{2}\rangle$	58.31
$\Gamma_8^{(3)}(c) = -0.131\|-\frac{9}{2}\rangle - 0.505\|-\frac{1}{2}\rangle - 0.258\|\frac{7}{2}\rangle + 0.813\|\frac{15}{2}\rangle$	58.31
$\Gamma_8^{(3)}(d) = 0.813\|-\frac{15}{2}\rangle - 0.258\|-\frac{7}{2}\rangle - 0.505\|0.5\rangle - 0.132\|\frac{9}{2}\rangle$	58.31
$\Gamma_7(e) = 0.191\|-\frac{9}{2}\rangle + 0.718\|-\frac{1}{2}\rangle + 0.331\|\frac{7}{2}\rangle + 0.582\|\frac{15}{2}\rangle$	57.42
$\Gamma_7(f) = 0.582\|-\frac{15}{2}\rangle + 0.331\|-\frac{7}{2}\rangle + 0.718\|\frac{1}{2}\rangle + 0.191\|\frac{9}{2}\rangle$	57.42
$\Gamma_6(g) = 0.633\|-\frac{13}{2}\rangle + 0.582\|-\frac{5}{2}\rangle - 0.451\|\frac{3}{2}\rangle - 0.239\|\frac{11}{2}\rangle$	15.74
$\Gamma_6(h) = -0.238\|-\frac{11}{2}\rangle - 0.451\|-\frac{3}{2}\rangle + 0.582\|\frac{5}{2}\rangle + 0.633\|\frac{13}{2}\rangle$	15.74
$\Gamma_8^{(2)}(i) = 0.018\|-\frac{15}{2}\rangle + 0.803\|-\frac{7}{2}\rangle - 0.239\|\frac{1}{2}\rangle - 0.546\|\frac{9}{2}\rangle$	12.80
$\Gamma_8^{(2)}(j) = -0.545\|-\frac{9}{2}\rangle - 0.239\|-\frac{1}{2}\rangle + 0.803\|\frac{7}{2}\rangle + 0.018\|\frac{15}{2}\rangle$	12.80
$\Gamma_8^{(2)}(k) = 0.234\|-\frac{13}{2}\rangle + 0.215\|-\frac{11}{2}\rangle - 0.148\|-\frac{5}{2}\rangle + 0.317\|-\frac{3}{2}\rangle + 0.101\|\frac{3}{2}\rangle - 0.468\|\frac{5}{2}\rangle + 0.068\|\frac{11}{2}\rangle + 0.737\|\frac{13}{2}\rangle$	12.80
$\Gamma_8^{(2)}(l) = 0.737\|-\frac{13}{2}\rangle - 0.068\|-\frac{11}{2}\rangle - 0.468\|-\frac{5}{2}\rangle - 0.101\|-\frac{3}{2}\rangle + 0.317\|\frac{3}{2}\rangle + 0.148\|\frac{5}{2}\rangle + 0.215\|\frac{11}{2}\rangle - 0.234\|\frac{13}{2}\rangle$	12.80
$\Gamma_8^{(1)}(m) = 0.007\|-\frac{15}{2}\rangle + 0.424\|-\frac{7}{2}\rangle - 0.415\|\frac{1}{2}\rangle + 0.805\|\frac{9}{2}\rangle$	0
$\Gamma_8^{(1)}(n) = 0.805\|-\frac{9}{2}\rangle - 0.415\|-\frac{1}{2}\rangle + 0.424\|\frac{7}{2}\rangle + 0.007\|\frac{15}{2}\rangle$	0
$\Gamma_8^{(1)}(o) = 0.939\|-\frac{11}{2}\rangle - 0.001\|-\frac{5}{2}\rangle - 0.278\|-\frac{3}{2}\rangle + 0.002\|\frac{3}{2}\rangle + 0.200\|\frac{5}{2}\rangle - 0.007\|\frac{11}{2}\rangle - 0.027\|\frac{13}{2}\rangle$	0
$\Gamma_8^{(1)}(p) = -0.026\|-\frac{13}{2}\rangle + 0.007\|-\frac{11}{2}\rangle + 0.200\|-\frac{5}{2}\rangle - 0.002\|-\frac{3}{2}\rangle - 0.278\|\frac{3}{2}\rangle + 0.001\|\frac{5}{2}\rangle + 0.939\|\frac{11}{2}\rangle$	0

with experimental data. Such an agreement confirms the validity of the crystal field parameters discussed above. Indeed, this good agreement reflects the lack of magnetic correlations observed since Er^{3+} in Ba_2ErSbO_6 behaves as a single ion with negligible interactions even at 70 mK.

5. Conclusion

Ba_2ErSbO_6 is shown through a systematic investigation to undergo no magnetic ordering or spin glass freezing down to 70 mK, despite a negative Curie–Weiss temperature of ∼5 K. The solved crystal field level scheme, which treats the magnetic Er^{3+} ion as a single ion, describes the observed experimental behaviour. As such, there are no appreciable interactions between the Er^{3+} ions on the fcc lattice. This can be attributed to the relatively large separation of the ions.

Acknowledgment

The work at Princeton University was supported by the NSF program in solid state chemistry.

References

[1] Ramirez A P 2001 *Handbook of Magnetic Materials* (Amsterdam: Elsevier)
[2] Moessner R 2001 *Can. J. Phys.* **79** 1283–91
[3] Bramwell S T and Gingras M J P 2001 *Science* **294** 1495–501

[4] Karunadasa H, Huang Q, Ueland B G, Schiffer P and Cava R J 2003 *Proc. Natl Acad. Sci.* **100** 8097–102
[5] Calder S *et al* 2010 Magnetic properties of Ba_2HoSbO_6 with a frustrated lattice geometry *Phys. Rev.* B **81** 064425
[6] Oguchi T, Nishimori N and Taguchi Y 1985 *J. Phys. Soc. Japan* **54** 4494–7
[7] Henley C L 1987 *J. Appl. Phys.* **61** 3962–4
[8] Diep H T and Kawamura H 1989 *Phys. Rev.* B **40** 7019–22
[9] Heinilä M T and Oja A S 1993 *Phys. Rev.* B **48** 16514–23
[10] Kuz'min E V 2003 *J. Exp. Theor. Phys.* **96** 129–39
[11] Bucher E, Guggenheim H J, Andres K, Hull G W and Cooper A S 1974 *Phys. Rev.* B **10** 2945–51
[12] Dunlap B D and Shenoy G L 1975 *Phys. Rev.* B **7** 2716–24
[13] Cheng C and Dorain P B 1976 *J. Chem. Phys.* **65** 785–91
[14] Fish G E, North M H and Stapleton H J 1980 *J. Chem. Phys.* **73** 4807–15
[15] Morley J P, Faulkner T R, Richardson F S and Schwartz R W 1981 *J. Chem. Phys.* **75** 539–60
[16] Morrison C A, Leavitt R P and Wortman D E 1980 *J. Chem. Phys.* **73** 2580–98
[17] Veenendaal E J, Brom H B and Huiskamp W J 1983 *Physica* B+C **121** 1–29
[18] Moon R M, Koehler W C, Child H R and Raubenheimer L J 1968 *Phys. Rev.* **176** 722–31
[19] Saines P J, Kennedy B J and Elcombe M M 2007 *J. Solid State Chem.* **180** 401–9
[20] Brown P J 2004 *International Tables for Crystallography* vol C pp 391–9
[21] Hutchings M T 1964 *Solid State Phys.* **16** 227–73
[22] Lea K R, Leask M J M and Wolf W P 1962 *J. Phys. Chem. Solids* **23** 1381–405
[23] Fabi P 1995 *ISIS Annual Report No* RAL-TR-95-023 (Rutherford Appleton Laboratory: ISIS Science Division) (ISSN 1358-6254)
[24] Dean J R and Bloor D 1972 *J. Phys. C: Solid State Phys.* **5** 2921–40
[25] Gruber J B, Henderson J R, Muramoto M, Rajnak K and Conway J G 1996 *J. Chem. Phys.* **45** 477–82
[26] Magnani N, Baraldi A, Buffagni E, Capelletti R, Mazzera M, Brovelli S and Lauria A 2007 *Phys. Status Solidi* **4** 1209–12
[27] Van Vleck J H 1932 *The Theory of Electric and Magnetic Susceptibilities* (Oxford: Clarendon)